

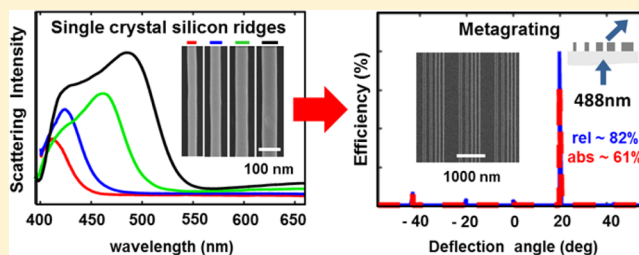
Visible Light Metasurfaces Based on Single-Crystal Silicon

David Sell,^{†,§} Jianji Yang,^{‡,§} Sage Doshay,^{†,§} Kai Zhang,^{‡,§} and Jonathan A. Fan^{*,‡}[†]Department of Applied Physics and [‡]Department of Electrical Engineering, Stanford University, Stanford, California 94305, United States

S Supporting Information

ABSTRACT: Semiconducting nanostructures are promising as components in high-performance metasurfaces. We show that single-crystal silicon can be used to realize efficient metasurface devices across the entire visible spectrum, ranging from 480 to 700 nm. Alternative forms of silicon, such as polycrystalline and amorphous silicon, suffer from higher absorption losses and do not yield efficient metasurfaces across this wavelength range. To demonstrate, we theoretically and experimentally characterize the resonant scattering peaks of individual single-crystal silicon nanoridges. In addition, we design high-efficiency metagratings and lenses based on nanoridge arrays, operating at visible wavelengths, using a stochastic optimization approach. We find that at wavelengths where single-crystal silicon is effectively lossless, devices based on high aspect ratio nanostructures are optimal. These devices possess efficiencies similar to those made of titanium oxide, which is an established material for high-efficiency visible wavelength metasurfaces. At blue wavelengths, where single-crystal silicon exhibits absorption losses, optimal devices are instead based on coupled low aspect ratio resonant nanostructures and are able to provide reasonably high efficiencies. We envision that crystalline silicon metasurfaces will enable compact optical systems spanning the full visible spectrum.

KEYWORDS: plasmonics, semiconductors, single crystal, silicon, visible light, metasurfaces, metamaterials



Metasurfaces are optical devices with amplitude and phase responses that can be tailored by design. For example, they can be engineered to control the wavefronts of incident electromagnetic waves¹ and support beam steering and focusing functionality^{2,3} with high efficiency. They can also manipulate the polarization and angular momentum of light^{4,5} in ways that exceed the capabilities of conventional optical components. Ultimately, the ability of metasurfaces to scale traditionally bulky optical parts down to ultrathin components promises to enable ultraminiaturized optical systems that will increase the scope and context of photonic applications.

There are two principal materials strategies to realizing metasurfaces. One is to use plasmonic materials, which possess a negative permittivity. Thus far, metals,^{6,7} doped semiconductors,^{8–10} transition metal oxides,¹¹ and transition metal nitrides¹² have been used in metasurfaces operating at wavelengths spanning the terahertz to visible. While this approach has produced workable devices, their overall efficiencies are limited by absorption losses intrinsic to plasmonic materials. The second strategy is to utilize low-loss, high refractive index semiconductors,¹³ which can be structured to support waveguiding¹⁴ or resonant scattering¹⁵ modes for amplitude and phase control. By limiting or eliminating absorption losses, this approach makes high-efficiency devices possible. For wavelengths spanning the infrared to visible range, materials such as amorphous and polycrystalline silicon^{16–18} have been utilized.

The push to realize metasurfaces that encompass the full visible spectrum, including blue wavelengths, has proven to be challenging. Amorphous and polycrystalline silicon nanostructures absorb significantly at these wavelengths, limiting their scattering efficiency. Aluminum is plasmonic above ultraviolet wavelengths,¹⁹ but its performance is limited by absorption losses and sensitivity to oxidization. Silicon nitride is transparent in the visible spectrum and has been utilized in metasurface designs,²⁰ but its low refractive index limits the efficiency of these devices. Thus far, the best demonstration of metasurfaces across the full visible regime has utilized titanium oxide,^{21,22} which has a refractive index of approximately 2.6 and is transparent. While this approach is effective, its implementation requires nonconventional fabrication methods.

In this Article, we show that single-crystal silicon can be adopted as a foundational material for high-efficiency visible light devices. This work builds on prior studies examining the optical properties of crystalline silicon nanoparticles²³ and nanowires,^{24–26} and it focuses on the implementation of crystalline silicon in metagratings and metasurfaces. At red and green wavelengths, the material behaves as an ideal, lossless high-index material, and established design strategies guided by intuitive physical constructs^{17,22} can be implemented. At blue wavelengths, the absorption losses in single-crystal silicon are no longer negligible. We focus our study on structures resonant

Received: June 25, 2016

Published: September 27, 2016

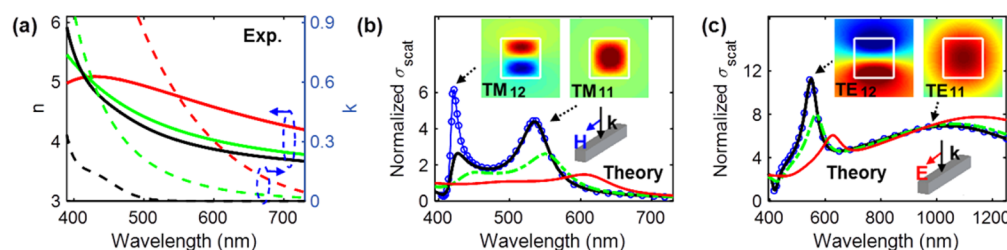


Figure 1. Optical properties of silicon nanoridges. (a) Complex refractive indices of single-crystal (black), polycrystalline (green), and amorphous (red) silicon, characterized experimentally by ellipsometry. The solid and dashed lines represent the real and imaginary parts, respectively, of the refractive index. (b) Calculated TM- and (c) TE-polarized scattering spectra of silicon nanoridges 90 nm wide and 90 nm high. The spectra are plotted in terms of normalized scattering cross-section for four variants of silicon: “ideal” (blue), single-crystal (black), polycrystalline (green), and amorphous silicon (red). The insets in (b) show the TM_{11} and TM_{12} mode profiles in terms of $\text{Re}(H_z)$, while the insets in (c) show the TE_{11} and TE_{12} mode profiles in terms of $\text{Re}(E_z)$.

at these wavelengths and find that in spite of non-negligible absorption losses metasurfaces with reasonable efficiencies can still be realized using advanced design algorithms. As such, single-crystal silicon is an effective material choice for high-performance metasurface devices across the entire visible wavelength range. We envision that the use of silicon will enable the integration of metasurface devices into existing technology platforms, due to the mainstream industrialization and mature development of silicon in electronics, on-chip photonics, and microelectromechanical systems.

We begin our analysis by quantifying the complex refractive index of single-crystal, polycrystalline, and amorphous silicon in the visible wavelength range (Figure 1a). This comparison between differing forms of silicon will help benchmark single-crystal silicon in the context of the other variants of silicon used in prior studies. Comparisons between single-crystal silicon and titanium oxide will come later, in our study of devices. Refractive index characterization is obtained by ellipsometry of thin film samples prepared using standard methods (see Methods section for details). The refractive indices measured here are consistent with those in the literature (Figure S1).

The plot shows that for all forms of silicon the real part of the refractive index is high throughout the visible spectrum, presenting the possibility of strong scattering in subwavelength-scale structures. However, the imaginary parts of the refractive indices are very different. Amorphous silicon has a pronounced imaginary component to its refractive index throughout the visible spectrum due to the disorder-induced broadening of its bands.²⁷ Polycrystalline silicon also has a significant imaginary refractive index due to material disorder at grain boundaries.²⁸ Single-crystal silicon, on the other hand, has no structural disorder and therefore possesses relatively low absorption below its direct band gap near 3.4 eV. At wavelengths longer than 500 nm, the imaginary part is nearly negligible, indicating that the material is effectively lossless at green and red wavelengths. At blue wavelengths between 450 and 500 nm, a small but non-negligible imaginary part to the refractive index arises.

It is not clear from an examination of the complex-valued refractive indices in which spectral ranges the varied forms of silicon can be used to produce high-efficiency metasurface devices. To address this issue, we analyze the scattering spectra of individual silicon nanoridges and their associated scattering modes. We select ridges with rectangular cross-sections as a model system for nano-optical engineering, as they have been widely utilized^{14,16,22} as metasurface building blocks. An analysis of devices will follow. We perform scattering spectra

calculations for four materials: “ideal,” single-crystal, polycrystalline, and amorphous silicon. We define “ideal” silicon to be a nonphysical reference material that has the real refractive index of single-crystal silicon but no imaginary part. Comparisons between “ideal” silicon with the other silicon variants will allow us to quantify the scattering efficiency of nanostructures made from those materials. The spectra are plotted in terms of the normalized scattering cross-section (σ_{scat}), which is the total scattering cross-section normalized by the geometric cross-section of the ridge.

Typical nanoridge scattering spectra, obtained here for 90 nm wide and 90 nm thick ridges, are plotted in Figure 1b and c. The excitation source is a plane wave with normal incidence to the ridges, and two incident polarizations are considered: TM-polarized light, in which the incident magnetic field is oriented parallel to the length of the ridge, and TE-polarized light, in which the incident electric field is oriented parallel to the length of the ridge. The modes are clearly visible as peaks in the “ideal” silicon spectra. The TM-polarized spectrum shows sharp TM_{11} and TM_{12} modes peaked near 560 and 420 nm, respectively, and the TE-polarized spectrum shows a sharp TE_{12} mode near 550 nm and an ultrabroad TE_{11} mode peaked near 1040 nm. The mode profiles of these resonances (insets of Figure 1b and c), calculated at their eigenfrequencies,²⁹ confirm their type and symmetry.

The single-crystal silicon nanoridge spectra, including the TE_{12} and TM_{11} mode peaks, overlap with those of “ideal” silicon at wavelengths longer than 500 nm, indicating that losses are negligible at these wavelengths. Below 500 nm, deviations occur due to absorption, and the TM_{12} mode at 420 nm has a peak magnitude that is reduced due to losses. Polycrystalline and amorphous silicon exhibit very different spectra due to absorption throughout the visible wavelength range. For both materials, the TE_{12} and TM_{11} modes are strongly suppressed, and the TM_{12} mode peaks are hardly visible.

It may be considered counterintuitive that single-crystal silicon can scatter light at wavelengths above 500 nm in ways that appear lossless. Silicon wafers are opaque to the eye, and conventional single-crystal silicon solar cells rely on strong absorption across the visible spectrum. In those cases, the silicon films are multiple micrometers thick, such that the small imaginary part of the refractive index contributes significant absorption. In our design regime, our structures are nanoscale and optically thin, minimizing the impact of material absorption.

The radiative characteristics of these modes can be inferred from the line widths of these resonances as calculated with “ideal” silicon, where radiative losses are the sole loss channel of the system. Modes with narrower line widths support stronger light–matter interactions, which result in enhanced absorption when material losses are added. The TE_{11} mode has an ultrabroad bandwidth and is highly radiative, with a quality factor $Q \approx 1$. Its radiative characteristics can be understood by its spatial delocalization from the silicon ridge (inset of Figure 1c). The TM_{12} , TM_{11} , and TE_{12} modes have much narrower bandwidths and possess Q factors of ~ 20 , 8, and 7, respectively. The TE_{12} mode supports a high Q because its two lobes are out of phase, yielding subradiant behavior. The TM_{11} mode is highly confined inside the subwavelength-scale silicon ridge and is therefore also subradiant. The TM_{12} mode is highly confined and possesses two out-of-phase lobes, yielding the highest Q of these modes.

To more systematically study the scattering properties of silicon nanostructures at visible frequencies, we calculate the TE- and TM-polarized scattering spectra for silicon nanoridges with a range of square cross-sectional dimensions. As the dimensions of the ridges change, the peak positions of the modes shift in wavelength. We record the peak wavelengths and corresponding σ_{scat} of the TE_{11} , TE_{12} , TM_{11} , and TM_{12} modes, for differently sized ridges. The results are summarized in Figure 2. For “ideal” silicon, σ_{scat} is high for all modes at all

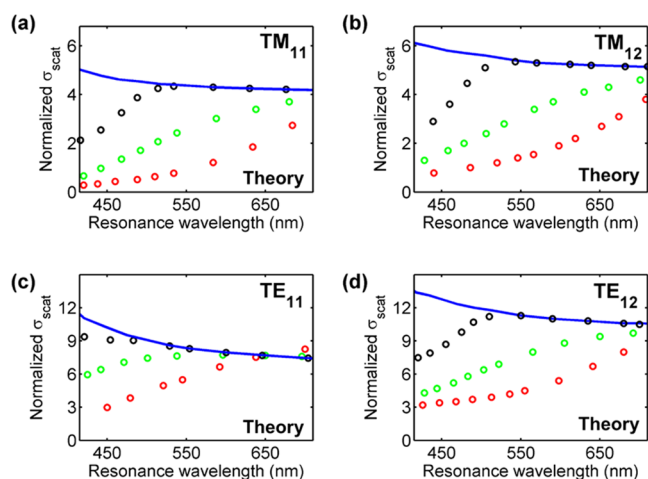


Figure 2. Theoretical analysis of the scattering properties of silicon nanoridges. (a, b) Plots of the peak normalized scattering cross-sections of silicon nanoridges under TM-polarized illumination for the (a) TM_{11} and (b) TM_{12} modes. The silicon nanoridges have square cross-sections, and the peak wavelengths of the modes are swept across the visible wavelength range by sweeping the cross-sectional dimensions. Data points are shown for “ideal” (blue line), single-crystal (black circles), polycrystalline (green circles), and amorphous silicon (red circles). (c, d) Plots of the peak normalized scattering cross-sections of silicon nanoridges under TE-polarized illumination for the (c) TE_{11} and (d) TE_{12} modes.

wavelengths, due to the high refractive index and lack of absorption in this material. σ_{scat} increases as the wavelength decreases for all modes, which follows from the dispersion of the refractive index of “ideal” silicon (Figure 1a).

For single-crystal silicon, the σ_{scat} 's above 500 nm match those of “ideal” silicon for all modes, confirming that the material can be effectively treated as lossless at these wavelengths. Below 500 nm, absorption causes the cross-

sections to deviate from those of “ideal” silicon. For the TE_{11} mode, this deviation is modest because the mode strongly radiates and is weakly localized within the silicon (Figure 1b, inset). At 450 nm, σ_{scat} for single-crystal silicon decreases by only 10% relative to that of “ideal” silicon. For the TE_{12} , TM_{11} , and TM_{12} modes, these deviations are larger due to their larger Q factors. For these modes, the σ_{scat} 's relative to those of “ideal” silicon decrease by 20% between 470 and 480 nm. As such, the scattering efficiencies of single-crystal silicon for modes of differing order and polarization are greater than 80% for wavelengths longer than 480 nm.

In sharp contrast, polycrystalline and amorphous silicon have substantially suppressed σ_{scat} 's for all modes throughout the visible wavelength range, due to absorption losses. This suppression is clearly visible with the TE_{11} mode, in spite of its strong radiative characteristics, and it is even more prominent in the high- Q TE_{12} , TM_{11} , and TM_{12} modes. As such, nanostructures fabricated from these materials do not efficiently scatter at visible wavelengths. It is noted that for amorphous silicon above 650 nm σ_{scat} of the TE_{11} mode exceeds that of ideal silicon, due to its larger real part of the refractive index (Figure 1a).

We note that while this analysis is performed for ridge geometries, it is general to other shapes common to metasurface engineering, such as cylinders, posts, and spheres, with and without a supporting substrate. The trends in normalized scattering cross-section and scattering efficiency for these geometries are consistent with our analysis above and are discussed in the Supporting Information.

Following our theoretical analysis, we experimentally study optical scattering from individual single-crystal and polycrystalline silicon nanoridges. The details of the fabrication process are in the Supporting Information. To summarize, single-crystal silicon samples are prepared by first bonding an SOI wafer to Pyrex using hydrogen silsesquioxane (HSQ) as an adhesive layer.³⁰ The silicon handle and buried oxide layer are then removed to expose the single-crystal silicon film, which is then patterned by electron beam lithography and etched. Scanning electron microscopy images of the ridges (Figure 3b, inset) indicate that they can be precisely etched with smooth

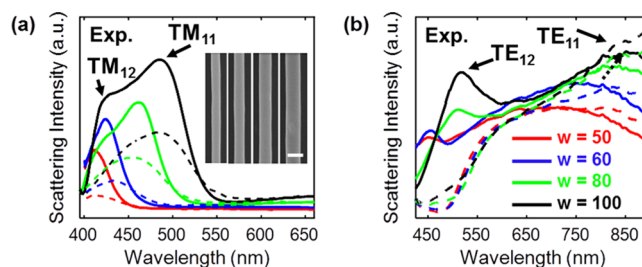


Figure 3. Scattering spectra of individual silicon nanoridges. (a) Dark-field scattering spectra of individual single-crystal (solid lines) and polycrystalline (dashed lines) silicon ridges for TM-polarized incident light. The ridge widths are 50 nm (red), 60 nm (blue), 80 nm (green), and 100 nm (black), and the thickness for all samples is 70 nm. Inset: Scanning electron microscopy images of single-crystal silicon ridges with widths of 50, 60, 80, and 100 nm (left to right). Scale bar: 100 nm. For imaging, the samples are coated with a thin layer of titanium to minimize charging, which artificially widens the ridges. (b) Dark-field scattering spectra of individual single-crystal (solid lines) and polycrystalline (dashed lines) silicon ridges for TE-polarized incident light.

sidewalls. Polycrystalline silicon samples are prepared by growing the silicon film on a silicon dioxide wafer by low-pressure chemical vapor deposition, followed by the same lithographic patterning and etching steps.

A polarized halogen white light source coupled to a near-normal dark-field spectroscopy setup³¹ is used to characterize light scattering from individual 10- μm -long ridges. Near-normal excitation is used instead of oblique excitation because it eliminates retardation effects, which can distort the spectral line shapes.

The spectra of 70-nm-thick ridges with differing widths, taken with differing incident polarizations, are plotted in Figure 3. The ridge widths range from 50 to 100 nm, and they are chosen so that the TM_{11} and TE_{12} modes of the ridges resonate at blue wavelengths. The spectra for TM-polarized incidence (Figure 3a) show that, as the ridge widths increase from 50 nm to 100 nm, the TM_{11} peak resonance wavelength shifts from 400 nm to 500 nm. For the 80-nm-wide ridge, the TM_{12} higher order mode emerges as a distinct feature near 415 nm and becomes further pronounced and red-shifted in the 100-nm-wide ridge. As such, crystalline silicon nanostructures can exhibit clear and distinct resonant features, including the fundamental and higher order modes, at blue wavelengths.

The spectra of polycrystalline silicon ridges are also plotted in Figure 3a and also show distinct peaks across the blue wavelength range. However, the magnitudes of these peaks are significantly lower than those from single-crystal silicon. For 50 and 60-nm-wide structures, the peaks have magnitudes that are 4 to 5 times lower than those from crystalline silicon. For 80 and 100-nm-wide structures, the peaks have magnitudes that are approximately half of those from single-crystal silicon. In addition, the polycrystalline silicon scattering spectra do not display any TM_{12} peaks, due to strong optical absorption.

The spectra of single-crystal silicon ridges excited by TE-polarized light are presented in Figure 3b. The TE_{11} fundamental modes peak at near-infrared frequencies for these ridges and shift from 750 nm to 900 nm as the ridge widths increase. The higher order TE_{12} mode, on the other hand, is more strongly confined and produces a clear narrow peak between 450 and 500 nm for these ridge geometries. The polycrystalline ridge spectra in Figure 3b display a clear TE_{11} mode peaked in the near-infrared. At these wavelengths, polycrystalline silicon has a larger real part of the refractive index compared to single-crystal silicon and therefore displays larger peak scattering magnitudes. However, no TE_{12} peaks are visible, due to absorption.

For the rest of our study, we focus on the implementation of devices based on coupled nanoridges. In the first part, we use silicon ridges as a base element to design and characterize beam deflectors, which are transmissive blazed grating structures that can deflect light at a specific angle and wavelength. These devices control the magnitude and phase of incident light in ways that can generalize to more complex metasurfaces, such as lenses.

There are multiple design strategies to producing optical responses from high refractive index nanostructures. One is to implement the structures as high aspect ratio dielectric waveguides with tunable phase delays.¹⁴ This route to phase control has a rich history spanning nearly 20 years and has applied binary grating design concepts to produce diffractive gratings^{32,33} and lenses.³⁴ More recently, these concepts have been revisited in the context of multifunctional devices¹⁷ operating at new wavelength regimes such as the visible.²² An

alternative strategy is to use coupled, low aspect ratio structures, which produce phase responses based on Mie resonant elements.^{2,35} Structures designed with this coupled Mie-scattering approach have advantages in ease of fabrication, especially at visible wavelengths where the widths of individual nanostructures scale down to the tens of nanometers range.

It is not obvious which of these two design approaches can produce better performing devices, especially with the presence of material absorption. In addition, the optimal design layouts for each approach are not intuitive. As such, we optimize and compare devices in the waveguide and Mie-scattering regimes using stochastic optimization. With this technique, we are able to solve for optimal device thicknesses, ridge widths, and ridge positions without any initial assumptions of the device geometry. We perform this analysis for devices that deflect TE-polarized light at a 20 degree angle. We optimize devices operating at 488 nm, where single-crystal silicon absorbs, and 633 nm, where single-crystal silicon is effectively lossless, and we compare single-crystal silicon devices with those made from titanium oxide. Our detailed methodology and final device dimensions are in the Supporting Information.

The angular distributions of transmitted radiation for optimized designs operating at 633 nm are plotted in Figure 4a–d, in terms of absolute and relative efficiency. Absolute

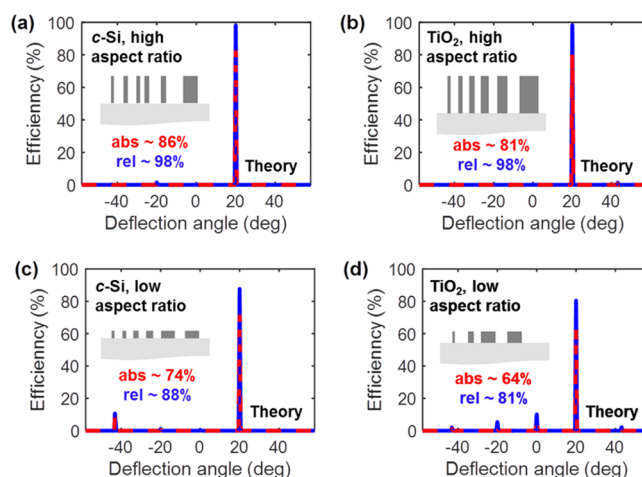


Figure 4. Far-field profiles of single-crystal silicon and titanium oxide devices deflecting normally incident 633 nm TE-polarized light at a 20 degree angle. (a, b) Waveguide-based devices designed using high aspect ratio (a) silicon and (b) titanium oxide nanoridges. (c, d) Mie-scattering-based devices designed using low aspect ratio (c) silicon and (d) titanium oxide nanoridges. In (a)–(d), the absolute and relative efficiencies are plotted using dashed red lines and solid blue lines, respectively.

efficiency is defined as the total power deflected into the desired angle divided by the total incident power. Relative efficiency is defined as the total power deflected into the desired angle divided by the total transmitted power. The results indicate that the high aspect ratio waveguide approach yields optimal device performance for both materials, which are lossless at this wavelength. Furthermore, the performances of optimized single-crystal silicon and titanium dioxide devices are comparable. In this design regime, the absolute efficiencies for both materials are in the 80–90% range and the relative efficiencies are 98%. Compared to device designs established in the literature,^{17,32} our devices exhibit similar absolute efficiencies and significantly higher relative efficiencies. These

improvements in performance are due to the flexibility of our optimization approach, which does not constrain the dielectric elements to discrete positions on a lattice.

In comparison, the low aspect ratio Mie-scattering devices for both materials are less optimal at this wavelength. For single-crystal silicon, the absolute and relative efficiencies are 74% and 88%, respectively, while the absolute and relative efficiencies of the titanium dioxide devices are 64% and 81%, respectively. The efficiencies of the silicon Mie-scattering devices are higher than those made from titanium oxide, due to its relatively large refractive index. Optimal efficiencies are achieved with high aspect ratio nanostructures because the coupling of incident light into these waveguide structures is efficient, with minimal back-reflection. The coupled Mie-scattering devices suffer from backscattering, which limits their performance.

At 488 nm, single-crystal silicon is no longer lossless, making material absorption a relevant parameter in device design. We find that with absorption the Mie-scattering approach yields silicon devices with higher absolute efficiency than those designed with the waveguide approach (Figure 5a,c): the absolute efficiencies of the Mie-scattering and waveguide-based devices are 65% and 54%, respectively. The relative efficiencies of both devices are comparable and in the 80–90% range. The waveguide-based devices are no longer optimal because these devices possess heights on the order of the operating

wavelength, which yields a relatively long absorption path length. The Mie-scattering structures possess deeply sub-wavelength-scale heights, reducing the total interaction between the light and the device and therefore minimizing absorption.

Titanium oxide remains lossless at 488 nm. The waveguide approach produces more efficient devices than those designed using the Mie-scattering approach, which is consistent with our analysis with 633 nm light (Figure 5b,d). In addition, these devices support higher efficiencies compared to those made from silicon. We note, however, that these optimal waveguide-based devices require nanostructures with aspect ratios with height-to-width dimensions on the order of 10:1, which presents a nontrivial fabrication challenge.

To experimentally test our design strategy at the absorbing blue end of the spectrum, we fabricate and characterize a single-crystal silicon deflector based on our optimized coupled Mie-scatterer scheme. The device is designed for TE-polarized 488 nm light and is 75 nm thick. The fabrication methodology is consistent with that for individual silicon ridges. A scanning electron microscopy image of the deflector (Figure 5e) shows a periodic array of coupled silicon ridges with clean sidewalls. To test the deflection efficiency, we collimate, filter, and polarize an incoherent white light source with a 488 nm laser line filter and then focus the light with a 0.14 NA objective onto the deflector. The transmitted beam is spatially filtered with a slit and characterized with a power meter mounted on a motorized rotation stage. The far-field profile of the transmitted light is displayed in Figure 5f. The plot shows that the device deflects the 488 nm beam at 20 degrees with absolute and relative efficiencies of 61% and 82%, respectively. A comparison between the theoretical (Figure 5c) and experimental (Figure 5f) deflection efficiencies shows very close agreement. A more quantitative analysis of the impact of the focusing objective NA and the slit on deflection efficiency is detailed in the Supporting Information.

Our optimization scheme can also be used to control the phase response of nanoscale optical elements, which serve as building blocks for metasurfaces in wavefront engineering applications. As a demonstration, we have optimized silicon nanoridge layouts that exhibit phase responses ranging from 0 to 2π at 488 nm (Figure 6a). By combining these structures into an array, we can construct metasurface devices with specific phase gradient profiles, such as a cylindrical lens (Figure 6b). With single-crystal silicon, our device possesses an absolute focusing efficiency of 64%, which is defined here as the fraction of incident light that focuses to the beam focal point. This efficiency metric is similar to that of our beam deflector.

We note that while our stochastic optimization approach provides one design methodology for nanoridge-based visible light metasurfaces, single-crystal silicon can be used in other alternative two- and three-dimensional design schemes. For example, it can be used in metasurface schemes that utilize cylindrical posts (Figure S10).

In conclusion, our study of silicon ridges and devices demonstrates that single-crystal silicon is a foundational material for metasurfaces spanning the full visible spectrum. For most of the visible wavelength range, single-crystal silicon is effectively lossless and can yield devices with performance metrics comparable to those made from titanium dioxide. At blue wavelengths, single-crystal silicon absorbs, but the material can still be used to construct devices with reasonably high efficiencies. Other variants of silicon, including polycrystalline and amorphous silicon, are not suitable at these wavelengths

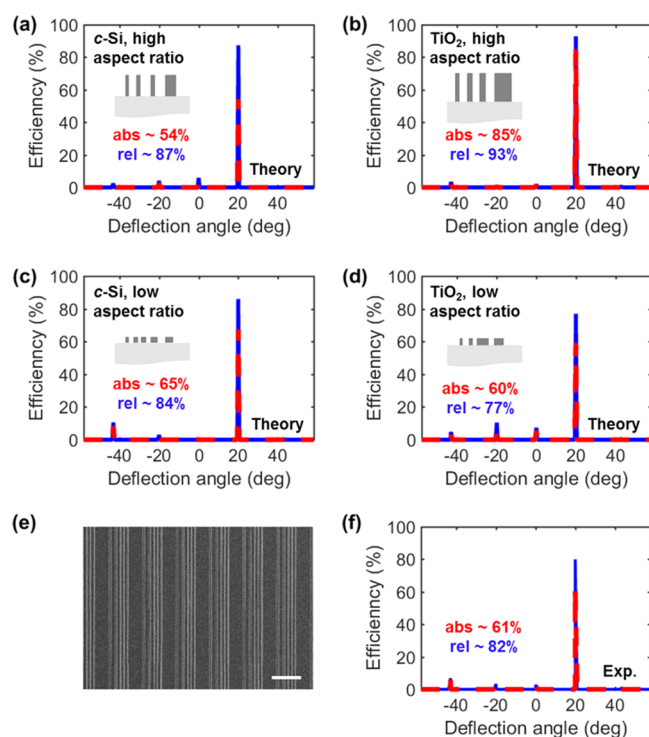


Figure 5. Far-field profiles of single-crystal silicon and titanium oxide devices deflecting normally incident 488 nm TE-polarized light at a 20 degree angle. (a, b) Devices designed using high aspect ratio (a) silicon and (b) titanium oxide nanoridges. (c, d) Devices designed using low aspect ratio (c) silicon and (d) titanium oxide nanoridges. (e) Scanning electron microscopy image of the single-crystal silicon deflector with the design from (c). Scale bar: 1 μm . (f) Far-field power measurement of TE-polarized 488 nm light passing through the deflector from (e). The absolute and relative efficiencies are measured to be 61% and 82%, respectively. In (a)–(d) and (f), the absolute and relative efficiencies are plotted using dashed red lines and solid blue lines, respectively.

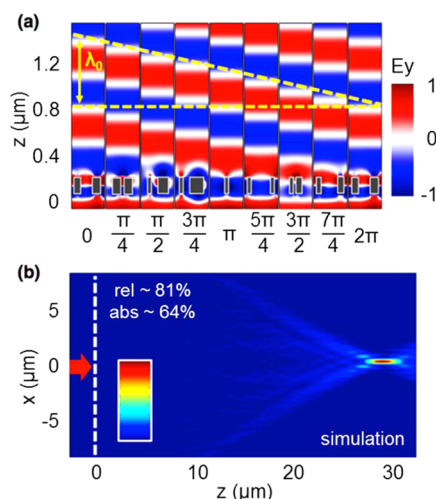


Figure 6. Single-crystal silicon metasurfaces with phase control. (a) Transmitted electric field wavefronts from metasurface elements optimized to yield phase responses ranging from 0 to 2π . The 150 nm tall silicon ridges are sketched as gray blocks, and the normally incident electromagnetic field is TE-polarized with a wavelength of 488 nm. (b) Field intensity profile of a cylindrical lens constructed using the elements in (a). The position of the lens is marked by the white dashed line. The width and focal length of the lens are 40 and 30 μm , respectively. The absolute and relative focusing efficiencies of the device are 64% and 81%, respectively.

due to material absorption losses. We also find, using stochastic optimization, that the optimal device design strategy depends on the wavelength of operation, which determines whether single-crystal silicon is lossless or absorbing. We note that these concepts in optimization can extend to fully three-dimensional layouts to produce devices with significantly better performance, and we will report these findings in future studies.

METHODS

Fabrication of the Crystalline Silicon Ridges and Gratings. A borosilicate glass substrate is spun-coat with hydrogen silesquioxane, prebaked, and held under vacuum for 20 min. A piece of SOI wafer (SOITEC) with a 100-nm-thick device layer is placed, with the device layer face down, on the coated wafer and bonded with a pressure of 2000 N at 400 $^{\circ}\text{C}$ for 1 h. The back-side silicon is removed by a combination of back-side polishing, etching with SF_6 , and etching with XeF_2 . The bottom oxide is removed by wet-etching in 2% HF. For thinner samples, the pieces are blanket dry-etched in C_2F_6 . The patterns are defined using electron beam lithography. Individual ridges are patterned using ma-N 2405 negative tone resist. Grating structures are patterned using ZEP 520A resist. The nanostructures are dry-etched using a breakthrough C_2F_6 etch, followed by a Cl_2 , HBr, and O_2 main etch, and finally an HBr and O_2 overetch.

Fabrication of the Polycrystalline and Amorphous Silicon Samples. Amorphous silicon is deposited using silane onto a fused silica substrate in a low-pressure chemical vapor deposition furnace at 525 $^{\circ}\text{C}$. Polycrystalline silicon is deposited using silane onto a fused silica substrate in a low-pressure chemical vapor deposition furnace at 620 $^{\circ}\text{C}$. The sample is optically characterized using ellipsometry to determine the final thickness and measure the refractive index. The complex refractive index fitting process includes a consistency check with the Kramers–Kronig relations. The

patterns in the p-Si are formed, etched, and characterized in the same manner as the crystalline silicon samples. Scanning electron microscopy images of individual polysilicon ridges are displayed in Figure S2.

Optical Simulation Methods. Finite-element simulations are performed using the scattered-field formulation of COMSOL Multiphysics 5.0. The computation volume is a sphere for 3D simulations and a circle for 2D simulations, each with a radius of $\sim 0.5\lambda$. The computation volume is surrounded by a PML layer with $\sim 0.5\lambda$ thickness, which eliminates backscattering. The outermost boundary of the PML is set as scattering boundary condition. The silicon resonators are positioned in the center of the computational window, with or without a semi-infinite substrate depending on the simulation.

Beam Deflector Optimization Methods. We optimize metasurfaces for beam deflection using a numerical thermal annealing approach. The computational foundation for our optimization scheme is rigorous coupled wave analysis (RCWA). This computation package is suitable for our application because it is fast and designed for periodic structures. Our structures are periodic, consist of infinitely long silicon nanoridges with a rectangular cross-section, and deflect light based on diffraction. The period determines the diffraction deflection angle and is predetermined. The refractive indices of single-crystal, polycrystalline, and amorphous silicon are taken to be those interpolated from experimental measurement (Figure 1a). We perform RCWA using the Reticolo software package for Matlab, written by the Lalanee group at the Institut d'Optique.³⁶

Our optimization routine involves an iterative process summarized in Figure S3. The optimization begins with a system consisting of uniformly spaced devices. A figure of merit is defined as the magnitude of power deflected from a plane wave into our desired deflection angle and is directly calculated using RCWA. During each subsequent iteration, a random perturbation is made to the system that involves shifting the width and/or location of all, some, or one of the scatterers. The new system is simulated, and the figure of merit is calculated. If the figure of merit does not improve, the change is rejected. If the figure of merit improves, the resulting device is used as the new starting configuration. The perturbation magnitudes are random variables with either Gaussian or normal distributions that decrease over the course of the optimization.

To identify optimal structures for waveguide-based and Mie-scatterer-based beam deflectors, parameter sweeps are performed for a wide range of ridge numbers (up to six per period) and ridge thicknesses. For each ridge number and thickness, hundreds of optimization simulations are performed, and we record the layout and efficiencies of the most optimal devices. A summary of our analysis of single-crystal silicon deflectors operating at 633 nm is displayed in Figure S4. The geometric parameters of the optimized devices presented in Figures 4 and 5 are summarized in Figure S5.

ASSOCIATED CONTENT

Supporting Information

The Supporting Information is available free of charge on the ACS Publications website at DOI: 10.1021/acsphotonics.6b00436.

Additional information (PDF)

AUTHOR INFORMATION

Corresponding Author

*E-mail: jonfan@stanford.edu.

Author Contributions

[§]D. Sell, J. Yang, S. Doshay, and K. Zhang contributed equally.

Notes

The authors declare no competing financial interest.

ACKNOWLEDGMENTS

The samples in this study were fabricated at the Stanford Nanofabrication Facility and Stanford Nano Shared Facility. This work was supported by the U.S. Air Force under Award Number FA9550-15-1-0161. D.S. was supported by the National Science Foundation (NSF) through the NSF Graduate Research Fellowship, and S.D. was supported by the Department of Defense through the National Defense Science and Engineering Graduate Fellowship Program. We acknowledge T. Kamins for useful discussions and R. Tiberio, M. Rincon, M. Mansourpour, J. Kruger, U. Raghuram, J. Conway, M. Stevens, and T. Brand for fabrication support.

REFERENCES

- (1) Yu, N.; Capasso, F. Flat Optics with Designer Metasurfaces. *Nat. Mater.* **2014**, *13*, 139–150.
- (2) Pfeiffer, C.; Grbic, A. Metamaterial Huygens' Surfaces: Tailoring Wave Fronts with Reflectionless Sheets. *Phys. Rev. Lett.* **2013**, *110*, 197401.
- (3) Aieta, F.; Genevet, P.; Kats, M. A.; Yu, N.; Blanchard, R.; Gaburro, Z.; Capasso, F. Aberration-Free Ultrathin Flat Lenses and Axicons at Telecom Wavelengths Based on Plasmonic Metasurfaces. *Nano Lett.* **2012**, *12*, 4932–4936.
- (4) Yu, N.; Genevet, P.; Kats, M. A.; Aieta, F.; Tetienne, J.-P.; Capasso, F.; Gaburro, Z. Light Propagation with Phase Discontinuities: Generalized Laws of Reflection and Refraction. *Science* **2011**, *334*, 333–337.
- (5) Ding, F.; Wang, Z.; He, S.; Shalaev, V. M.; Kildishev, A. V. Broadband High-Efficiency Half-Wave Plate: A Supercell-Based Plasmonic Metasurface Approach. *ACS Nano* **2015**, *9*, 4111–4119.
- (6) Zheludev, N. I.; Kivshar, Y. S. From Metamaterials to Metadevices. *Nat. Mater.* **2012**, *11*, 917–924.
- (7) Kildishev, A. V.; Boltasseva, A.; Shalaev, V. M. Planar Photonics with Metasurfaces. *Science* **2013**, *339*, 1232009. [10.1126/science.1232009](https://doi.org/10.1126/science.1232009)
- (8) Chen, H.-T.; Padilla, W. J.; Zide, J. M. O.; Gossard, A. C.; Taylor, A. J.; Averitt, R. D. Active Terahertz Metamaterial Devices. *Nature* **2006**, *444*, 597–600.
- (9) Law, S.; Yu, L.; Rosenberg, A.; Wasserman, D. All-Semiconductor Plasmonic Nanoantennas for Infrared Sensing. *Nano Lett.* **2013**, *13*, 4569–4574.
- (10) Iyer, P. P.; Butakov, N. A.; Schuller, J. A. Reconfigurable Semiconductor Phased-Array Metasurfaces. *ACS Photonics* **2015**, *2*, 1077–1084.
- (11) Feigenbaum, E.; Diest, K.; Atwater, H. A. Unity-Order Index Change in Transparent Conducting Oxides at Visible Frequencies. *Nano Lett.* **2010**, *10*, 2111–2116.
- (12) Naik, G. V.; Kim, J.; Boltasseva, A. Oxides and Nitrides as Alternative Plasmonic Materials in the Optical Range. *Opt. Mater. Express* **2011**, *1*, 1090–1099.
- (13) Jahani, S.; Jacob, Z. All-Dielectric Metamaterials. *Nat. Nanotechnol.* **2016**, *11*, 23–36.
- (14) Khorasaninejad, M.; Capasso, F. Broadband Multifunctional Efficient Meta-Gratings Based on Dielectric Waveguide Phase Shifters. *Nano Lett.* **2015**, *15*, 6709–6715.
- (15) Staude, I.; Miroshnichenko, A. E.; Decker, M.; Fofang, N. T.; Liu, S.; Gonzales, E.; Dominguez, J.; Luk, T. S.; Neshev, D. N.; Brener, I.; Kivshar, Y. Tailoring Directional Scattering through Magnetic and Electric Resonances in Subwavelength Silicon Nanodisks. *ACS Nano* **2013**, *7*, 7824–7832.
- (16) Lin, D.; Fan, P.; Hasman, E.; Brongersma, M. L. Dielectric Gradient Metasurface Optical Elements. *Science* **2014**, *345*, 298–302.
- (17) Arbabi, A.; Horie, Y.; Bagheri, M.; Faraon, A. Dielectric Metasurfaces for Complete Control of Phase and Polarization with Subwavelength Spatial Resolution and High Transmission. *Nat. Nanotechnol.* **2015**, *10*, 937–943.
- (18) Arbabi, A.; Horie, Y.; Ball, A. J.; Bagheri, M.; Faraon, A. Subwavelength-Thick Lenses with High Numerical Apertures and Large Efficiency Based on High-Contrast Transmitarrays. *Nat. Commun.* **2015**, *6*, 706910. [10.1038/ncomms8069](https://doi.org/10.1038/ncomms8069)
- (19) Knight, M. W.; King, N. S.; Liu, L.; Everitt, H. O.; Nordlander, P.; Halas, N. J. Aluminum for Plasmonics. *ACS Nano* **2014**, *8*, 834–840.
- (20) Zhan, A.; Colburn, S.; Trivedi, R.; Fryett, T. K.; Dodson, C. M.; Majumdar, A. Low-Contrast Dielectric Metasurface Optics. *ACS Photonics* **2016**, *3*, 209.
- (21) Byrnes, S. J.; Lenef, A.; Aieta, F.; Capasso, F. Designing Large, High-Efficiency, High-Numerical-Aperture, Transmissive Meta-lenses for Visible Light. *Opt. Express* **2016**, *24*, 5110–5124.
- (22) Khorasaninejad, M.; Chen, W. T.; Devlin, R. C.; Oh, J.; Zhu, A. Y.; Capasso, F. Metalenses at Visible Wavelengths: Diffraction-Limited Focusing and Subwavelength Resolution Imaging. *Science* **2016**, *352*, 1190–1194.
- (23) Fu, Y. H.; Kuznetsov, A. I.; Miroshnichenko, A. E.; Yu, Y. F.; Luk'yanchuk, B. Directional Visible Light Scattering by Silicon Nanoparticles. *Nat. Commun.* **2013**, *4*, 1527.
- (24) Brönstrup, G.; Jahr, N.; Leiterer, C.; Csáki, A.; Fritzsche, W.; Christiansen, S. Optical Properties of Individual Silicon Nanowires for Photonic Devices. *ACS Nano* **2010**, *4*, 7113–7122.
- (25) Seo, K.; Wober, M.; Steinvurzel, P.; Schonbrun, E.; Dan, Y.; Ellenbogen, T.; Crozier, K. B. Multicolored Vertical Silicon Nanowires. *Nano Lett.* **2011**, *11*, 1851–1856.
- (26) Cao, L.; Fan, P.; Barnard, E. S.; Brown, A. M.; Brongersma, M. L. Tuning the Color of Silicon Nanostructures. *Nano Lett.* **2010**, *10*, 2649–2654.
- (27) Cody, G. D.; Tiedje, T.; Abeles, B.; Brooks, B.; Goldstein, Y. Disorder and the Optical-Absorption Edge of Hydrogenated Amorphous Silicon. *Phys. Rev. Lett.* **1981**, *47*, 1480–1483.
- (28) Jackson, W. B.; Johnson, N. M.; Biegelsen, D. K. Density of Gap States of Silicon Grain Boundaries Determined by Optical Absorption. *Appl. Phys. Lett.* **1983**, *43*, 195–197.
- (29) Bai, Q.; Perrin, M.; Sauvan, C.; Hugonin, J. P.; Lalanne, P. Efficient and Intuitive Method for the Analysis of Light Scattering by a Resonant Nanostructure. *Opt. Express* **2013**, *21*, 27371–27382.
- (30) Chung, J. W.; Jae-kyu, L.; Piner, E. L.; Palacios, T. Seamless On-Wafer Integration of Si(100) MOSFETs and GaN HEMTs. *IEEE Electron Device Lett.* **2009**, *30*, 1015–1017.
- (31) Fan, J. A.; Bao, K.; Lassiter, J. B.; Bao, J.; Halas, N. J.; Nordlander, P.; Capasso, F. Near-Normal Incidence Dark-Field Microscopy: Applications to Nanoplasmonic Spectroscopy. *Nano Lett.* **2012**, *12*, 2817–2821.
- (32) Lalanne, P.; Astilean, S.; Chavel, P.; Cambil, E.; Launois, H. Design and Fabrication of Blazed Binary Diffractive Elements with Sampling Periods Smaller than the Structural Cutoff. *J. Opt. Soc. Am. A* **1999**, *16*, 1143–1156.
- (33) Larouche, S.; Smith, D. R. Reconciliation of generalized refraction with diffraction theory. *Opt. Lett.* **2012**, *37*, 2391–2393.
- (34) Mait, J. N.; Scherer, A.; Dial, O.; Prather, D. W.; Gao, X. Diffractive lens fabricated with binary features less than 60 nm. *Opt. Lett.* **2000**, *25*, 381–383.
- (35) Aieta, F.; Kats, M. A.; Genevet, P.; Capasso, F. Multiwavelength Achromatic Metasurfaces by Dispersive Phase Compensation. *Science* **2015**, *347*, 1342–1345.
- (36) Hugonin, J. P.; Lalanne, P. *Reticolo Software for Grating Analysis*; Institut d'Optique: Orsay, France, 2005.